ACS Catalysis

Research Article

pubs.acs.org/acscatalysis

Mesoporous MFI Zeolite Nanosponge as a High-Performance Catalyst in the Pechmann Condensation Reaction

Jeong-Chul Kim,[†,‡] Ryong Ryoo,[†,‡,§] Maksym V. Opanasenko,[∥,⊥] Mariya V. Shamzhy,[∥,⊥] and Jiří Čejka*[,∥]

[†]Center for Nanomaterials and Chemical Reactions, Institute for Basic Science (IBS), Daejeon 305-701, Republic of Korea

[‡]Graduate School of Nanoscience and Technology, KAIST, Daejeon 305-701, Republic of Korea

[§]Department of Chemistry, KAIST, Daejeon 305-701, Republic of Korea

[∥]J. Heyrovský Institute of Physical Chemistry, Academy of Sciences of Czech Republic, v.v.i., Dolejškova 3, 182 23 Prague 8, Czech Republic

[⊥]Department of Porous Materials, L.V. Pisarzhevskiy Institute of Physical Chemistry, National Academy of Sciences of Ukraine, Pr. Nauky 31, 03028 Kiev, Ukraine

Supporting Information

ABSTRACT: A zeolite nanosponge possessing **MFI** framework type was hydrothermally prepared by a seed-assisted synthesis method using $C_{22}H_{45}-N^+(CH_3)_2-C_6H_{12}-N^+(CH_3)_2-C_6H_{13}$ as a structure-directing agent. The nanosponge morphology was composed of a three-dimensional disordered network of **MFI** nanolayers with 2.5 nm thickness supporting each other. Catalytic performance of the **MFI** nanosponge was investigated in the Pechmann condensation of bulky reactants (pyrogallol and resorcinol) with ethyl acetoacetate and compared with conventional zeolites **MFI**, **BEA**, and USY) and also layered **MFI**, pillared **MFI**, and self-pillared **MFI**. The investigation revealed outstanding catalytic performance of the **MFI** nanosponge, which can be attributed to the contribution of strong acid sites located on the external surfaces accessible for the reaction of bulky reactants.

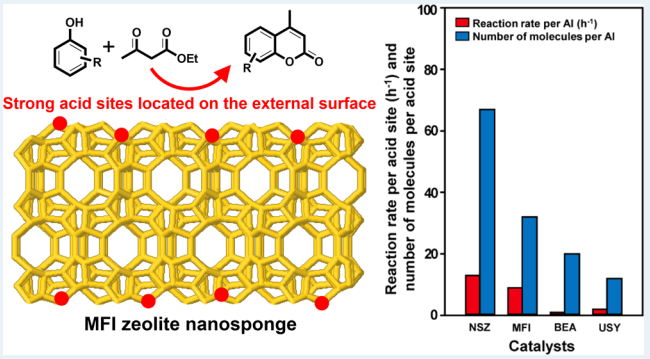

KEYWORDS: *nanomorphic zeolite, **MFI**, hierarchical zeolite, external acidity, Pechmann reaction, mesoporous material*

1. INTRODUCTION

The Pechmann reaction is one of the important condensation reactions to produce coumarins from activated phenols with β-ketoesters or unsaturated carboxylic acids.[1] The products are widely used as key intermediates in the pharmaceutical, agrochemical, and fragrance industries.[2−4] The Pechmann reaction proceeds via an acid-catalyzed transesterification, keto−enol tautomerisation, Michael addition, and an acid-catalyzed dehydration.[5] In the Pechmann reaction, H_2SO_4, $AlCl_3$, P_2O_5, and CF_3COOH are used as conventional catalysts.[6−8] Their major drawback is the need to use large quantities of catalysts to get high yields of products (e.g., 10−12 equiv of H_2SO_4 and 3−4 equiv of CF_3COOH).[9] The use of these catalysts is complicated by corrosion, toxicity, separation, and recovery. In principle, these homogeneous catalysts can be replaced by heterogeneous solid catalysts such as Nafion-H, amberlyst, zeolites, heteropoly acids, metal oxide, inorganic ion exchangers, and functionalized mesoporous silica.[10−15] Among them, zeolites have received considerable attention due to their strong Brønsted and Lewis acid sites, shape selectivity, high stability, and easy regenerability.[10]

Conventional zeolite catalysts often cause diffusion limitations of bulky aromatic reactants and products due to their small micropore openings. To minimize the diffusion problems on the conventional zeolites, large-pore zeolites (12-ring, e.g., **BEA** and USY) and extra-large pore zeolite (14-ring, e.g., **UTL**) are typically chosen for the Pechmann condensation reactions.[16,17] However, even large and extra-large pore zeolites still have micropores smaller than 1.0 nm, resulting in diffusion limitations for bulky molecules in Pechmann condensation. Recently, metal organic frameworks (MOFs) with extra-high porosity and regular arrangement of a large number of active sites were used as catalysts for various types of condensation reactions. In particular, Cu-benzene-1,3,5-tricarboxylate (Cu-BTC) and Fe-benzene-1,3,5-tricarboxylate (Fe-BTC) exhibited higher catalytic performance in the 1-naphthol condensation reaction than conventional beta and USY zeolites due to the regularity in the arrangement of active sites within the Cu-BTC and Fe-BTC frameworks.[17] However, catalytic activity of the MOF for pyrogallol condensation was poor. This result was attributed to the low stability of MOFs framework interacting with pyrogallol molecules.

Received: December 16, 2014
Revised: February 12, 2015
Published: March 11, 2015

DOI: 10.1021/cs502021a
ACS Catal. 2015, 5, 2596−2604

In 2009, mesoporous **MFI** zeolite with lamellar structure was reported by Ryoo and co-workers.[18] They discovered a hydrothermal synthesis protocol to produce hierarchically porous zeolites of ultrathin (<5 nm) framework thicknesses using surfactants as dual structure-directing agent (SDA) in the micro and meso scales. Typically, **MFI** zeolite nanosheets of 2.5 nm thickness were synthesized in the form of multilamellar mesostructure or a disordered assembly possessing broad distribution of mesopores, using $C_{22}H_{45}-N^+(CH_3)_2-C_6H_{12}-N^+(CH_3)_2-C_6H_{13}$. Recently, the hydrothermal synthesis method was modified by the addition of bulk **MFI** zeolite as seeds.[19] This seed-assisted method allowed rapid synthesis of the nanosheet zeolite with nanosponge morphologies. The nanosponge zeolite (NSZ in short) was composed of three-dimensional disordered network of **MFI** nanolayers with 2.5 nm thickness, exhibiting a narrow distribution of mesopore diameters centered at ∼4 nm.[20] The **MFI** NSZ exhibited high catalytic activity and long lifetime in the liquid-phase Friedel–Crafts alkylation and acylation of aromatics and annulation of phenols with 2-methyl-3-buten-2-ol.[21−23] This indicated that the **MFI** nanosheets in NSZ contained a large number of strong Brønsted acid sites on the external surfaces. The role of external acid sites in layered zeolites was recently reviewed by Pastore,[24] Roth,[25] and Corma.[26]

In this contribution, we investigated the performance of the **MFI** NSZ as a catalyst in Pechmann condensation reaction of phenols (pyrogallol and resorcinol) with ethyl acetoacetate. The results are discussed in comparison with the catalytic performance of conventional zeolites (**MFI**, **BEA**, and USY) and layered **MFI** zeolites of different textural properties (lamellar, pillared, and self-pillared **MFI**).

2. EXPERIMENTAL SECTION

2.1. Catalyst Preparation. The **MFI** NSZ was synthesized following the seed-assisted hydrothermal synthesis method using $[C_{22}H_{45}-N(CH_3)_2-C_6H_{12}-N(CH_3)_2-C_6H_{13}]$ Br_2 (in short, "C_{22-6-6}") as a SDA, as described elsewhere.[21] At first, different amounts of aluminum sulfate $[Al_2(SO_4)_3$ 18 H_2O, 98%, Sigma–Aldrich] were dissolved in distilled water to vary the concentration of Al in the final zeolite. This solution was added into an aqueous NaOH solution containing the C_{22-6-6} surfactant and stirred for 1 h at room temperature. Then, water glass (SiO_2 = 29 wt %, Si/Na = 1.75, Shinheung Chemical) was added dropwise with continuous stirring. After stirring the resultant gel at 333 K for 2 h, a commercial **MFI** zeolite (Zeolyst, CBV 8014, Si/Al = 40) amounting to 5 wt % of the total silica source was added as a seed. The final synthesis gel had a composition of 100 SiO_2/ n Al_2O_3/ 7.5 C_{22-6-6}/ 30 Na_2O/21 H_2SO_4/ 5000 H_2O in mole ratios, where n = 1, 2, or 4. The synthesis gel was further stirred for 6 h at 333 K and then heated for 2.5 days at 413 K in a Teflon-lined autoclave equipped with a magnetic stirrer. The solid product crystallized in the autoclave was filtered, washed by water, and dried in an oven at 373 K for 12 h. The zeolite sample is denoted as NSZ-x, according to the Si/Al ratio (x = 22, 48 or 95) determined by the elemental analysis using inductively coupled plasma atomic emission spectroscopy (ICP-AES) using an OPTIMA 4300 DV instrument (PerkinElmer).

Layered **MFI** zeolites were hydrothermally synthesized following the procedures reported in the literature.[27−29] Lamellar **MFI** and pillared **MFI** zeolites were synthesized using the C_{22-6-6} SDA. Tetraethylorthosilicate (TEOS, 95%, Junsei) was used as the silica source. Sodium aluminate (53 wt %, Sigma-Aldrich) was the alumina source. The details of the synthesis conditions are same as described in refs 27,28. For self-pillared **MFI**, the SDA was tetra-*n*-butyl phosphonium hydroxide solution (TBPOH, 40 wt %, Sigma-Aldrich). TEOS (95%, Junsei) was used as the silica source. Aluminum isopropoxide (Sigma-Aldrich) was the alumina source. The details of the synthesis procedure are described in ref 29.

All synthesized zeolite samples were calcined in air at 823 K, and then ion-exchanged to the NH_4^+ form by slurring in a 1-M NH_4NO_3 aqueous solution containing NH_4^+ corresponding to 3-fold access of NH_4^+ with respect to Al content in zeolite. The treatment with NH_4NO_3 solution was repeated three times, in order to maximize the ion-exchange level. Subsequently, the NH_4^+-exchanged zeolites were calcined again in air at 823 K for conversion to the H^+-ionic form.

Conventional H-**BEA** (CP814E), H-**MFI** (CBV 3024E), and H-USY (CBV 720) zeolites were purchased from Zeolyst and calcined at 823 K before use.

2.2. Characterization. Powder X-ray diffraction (XRD) patterns were measured with a Rigaku Multiflex diffractometer using Cu Kα radiation (30 kV, 40 mA). The nitrogen sorption isotherms were measured at liquid argon temperature (87 K) with a Micromeritics Tristar II instrument. Si/Al ratios were determined by inductively coupled plasma-atomic emission spectroscopy (ICP/AES) using an OPTIMA 4300 DV instrument (PerkinElmer). Scanning electron micrographs (SEM) images were taken with a Verios SEM microscope operating at 1 kV (decelerating voltage: 3.0 kV) without a metal coating. Transmission electron micrographs (TEM) images were obtained using an aberration-corrected Titan ETEM G^2 at an operating voltage of 300 kV.

The concentration of Lewis (c_L) and Brønsted (c_B) acid sites was determined after adsorption of pyridine (Py) by FTIR spectroscopy using a Nicolet Protégé 460 Magna with a transmission MCT/A detector. Zeolite samples were pressed into self-supporting wafers with a density of 8.0−12 mg cm^{-2} and activated in situ at T = 723 K and P = 5 × 10^{-5} Torr for 4 h. Pyridine adsorption was carried out at 423 K for 20 min at a partial pressure of 3.5 Torr, followed by desorption for 20 min at the same temperature. Pyridine was purified through freezing–pump–thaw cycles. All spectra were recorded with a resolution of 4 cm^{-1} by collecting 128 scans for a single spectrum at room temperature. Spectra were normalized to a wafer density of 10 mg cm^{-2}. Concentration of c_L and c_B were evaluated from the integral intensities of bands at 1454 cm^{-1} (Lewis acid sites - c_L) and at 1545 cm^{-1} (Brønsted acid sites - c_B) using extinction coefficients, ε(L) = 2.22 cm μmol^{-1}, and ε(B) = 1.67 cm μmol^{-1}.[30] A relatively large probe molecule 2,6-di-*tert*-butyl-pyridine (DTBP) was used to determine the accessibility of acid sites in the prepared zeolites.[31] The adsorption of DTBP took place at 423 K for 15 min at an equilibrium vapor pressure of the probe molecule. Desorption proceeded at the same temperature for 1 h followed by collection of spectra at room temperature. Extinction coefficients determined in ref 30 were used for the evaluation of c_B adsorbing DTBP.

2.3. Catalytic Measurements. Pechmann condensation reaction of phenols (pyrogallol and resorcinol) with ethyl acetoacetate was performed in a liquid phase using a multiexperiment StarFish workstation (Radley's Discovery Technologies U.K.). Prior to condensation reaction, 0.1 g of the H^+ form of a catalyst was activated at 673 K for 90 min in a stream of air. After cooling the catalyst to 473 K, phenol (5

DOI: 10.1021/cs502021a
ACS Catal. 2015, 5, 2596−2604

mmol), *n*-dodecane (0.5 g, internal standard), and the catalyst were added to the three-neck vessel. The reactor was equipped with a condenser and thermometer and heated to the reaction temperature (393 or 423 K). When the desired reaction temperature was reached, ethyl acetoacetate (10 mmol) was added into the reaction vessel. Aliquots of the reaction mixture were sampled from the reactor at various reaction times. The mixtures were rapidly cooled to room temperature to quench the reaction and separated by centrifugation to remove the catalyst. The liquid part was analyzed on a gas chromatograph (Agilent 6850), which was equipped with a flame ionization detector and a HP-1 column (Agilent, 30 m long, 0.25 mm ID, and 0.2 μm thick coating). The conversion and selectivity were calculated on the basis of a GC analysis.

2.4. Recycle Test. Recyclability of the zeolite catalyst was investigated in the case of pyrogallol condensation with ethyl acetoacetate. After 30 h of reaction, the catalyst was collected by filtration. The used catalyst was dried at 333 K for 6 h and calcined at 823 K for 6 h in a stream of air to remove the organic content. For the qualitative analysis of the organic residues in the catalyst, the organic-zeolite composite was first treated with 15% HF (aq) at room temperature for 6 h in Teflon flask to dissolve zeolite framework. After neutralizing the acidic solution with NaOH aqueous solution, CH_2Cl_2 was added to extract organic species from the water phase. The organic phase was analyzed by GC-mass analyzer (Thermo-Finnigan, FOCUS DSQ II Single Quadrupole) to identify the organic species that existed in the used catalyst.

3. RESULTS AND DISCUSSION

3.1. Improved External Acidity of Nanosponge MFI Zeolite. Figure 1 shows representative SEM and TEM images of **MFI** zeolite nanosponge samples synthesized using C_{22-6-6} surfactant and **MFI** zeolite seeds. The NSZ samples exhibit a nanosponge-like morphology, which consists of highly crystalline **MFI** nanolayers. The zeolitic nanolayers have a 2.5 nm thickness along the crystal *b*-axis with somewhat preferred orientation in parallel. The nanolayers are self-connected through crystalline pillars into a three-dimensional disordered network. All nanosponge samples exhibit very similar morphologies. No significant presence of any amorphous particles, bulk **MFI** zeolite particles or other impurities was detected in the NSZ samples upon investigation using SEM, TEM, and XRD.

Figure 2a shows the XRD patterns of the NSZ samples. All the nanosponge samples exhibited the characteristic Bragg reflections corresponding to the **MFI** zeolite structure in the wide angle region above $2\theta = 5°$. The peak intensities and their sharpness decreased in the order of NSZ-95 > NSZ-48 > NSZ-22, which is consistent with decreasing Al contents in the zeolite. This result can be attributed to decreasing lengths of individual zeolite nanosheets constituting the nanosponge morphology as Al content of the zeolite increased, and this is in good agreement with previous work reported by Jo et al.[19] Another notable feature of the XRD pattern is a small-angle peak with low intensity around $2\theta = 1.5°$. This feature is due to the structural correlation between nearest neighboring nanosheets in the case of NSZ with preferred orientation of nanosheets. The structural correlation became weaker as the Al content increased, due to the formation of more irregular sponge network with shorter nanosheets. As a result, the small-angle reflection peak in the case of NSZ-22 was indistinguishable from the strong background intensity.

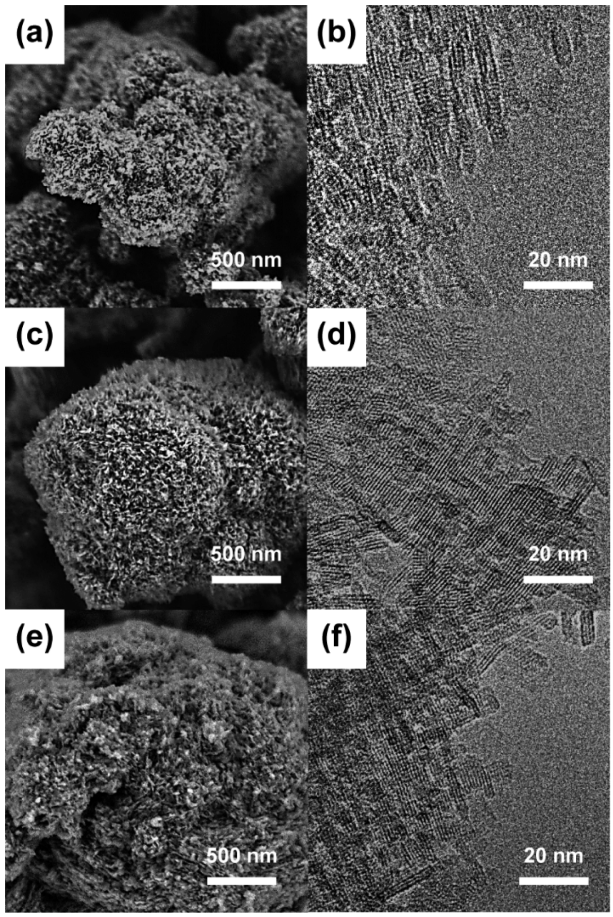

Figure 1. SEM (left column) and TEM (right column) images of NSZ-22 (a, b), NSZ-48 (c, d) and NSZ-95 (e, f).

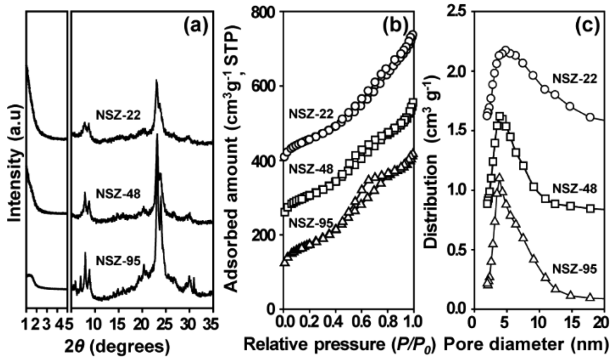

Figure 2. Powder XRD patterns (a), nitrogen adsorption isotherms (b), and BJH pore size distribution corresponding to the adsorption branch (c) of NSZ-22, NSZ-48, and NSZ-95. The isotherms for NSZ-48 and NSZ-22 were offset vertically by 150 and 300 $cm^3\ g^{-1}$ STP, respectively.

Nitrogen adsorption isotherms of NSZ samples at 77 K are shown in Figure 2. The adsorption isotherms of NSZ exhibit a combination of type I and IV isotherms with a sharp increase in the adsorbed amount in the range of $0.4 < P/P_0 < 0.5$. This increase is attributed to the capillary condensation in interparticle space among zeolitic nanolayers. This is a typical characteristic of the disordered mesoporous structures.[32] However, NSZ-*x* samples show different hysteresis loops in the range of $0.4 < P/P_0 < 0.9$. For NSZ-22 sample, the hysteresis loops have the general type H3 form, corresponding

DOI: 10.1021/cs502021a
ACS Catal. 2015, 5, 2596−2604

to slit-shaped pores. This can be related to the synthetic procedure applied. In the case of NSZ-48 and NSZ-95, the hysteresis loops are type H2 associated with ink-bottle shaped pores. The adsorption isotherm was analyzed using Barrett–Joyner–Halenda (BJH) algorithm evidencing a narrow distribution of mesopore diameters centered at 4 nm with large pore volume for all the NSZ samples (0.56–0.63 cm^3 g^{-1}). This mesoporosity of the NSZ samples is comparable to that of ordered mesoporous silicas such as MCM-41 and SBA-15 (mesopore volume 0.6 cm^3 g^{-1}, mesopore diameter 4.1 nm).[33,34] Similar mesoscale pore-generating effects can be assumed between NSZ and MCM-41 molecular sieves, taking into account the resemblance of the organic mesopore-generating part (surfactant tails) commonly used for the synthesis of MCM-41 and NSZ materials, as well as similarity of their textural properties. All NSZ samples possess high specific BET areas (510–610 cm^2 g^{-1}) and external surface areas (350–370 cm^2 g^{-1}) determined by the *t*-plot method.[35] This result is in a good agreement with the highly mesoporous texture of NSZ samples.

Figure 3 shows SEM images and XRD patterns of conventional **MFI**, **BEA**, and **FAU** (USY) zeolites. The XRD

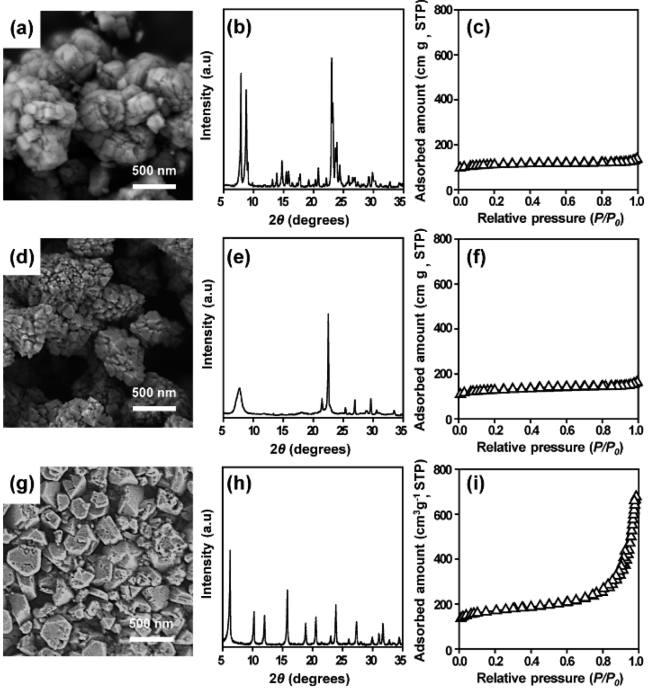

Figure 3. SEM images of **MFI** (a), **BEA** (d), and USY (g). Powder XRD patterns of **MFI** (b), **BEA** (e), and USY (h). Nitrogen adsorption isotherm of **MFI** (c), **BEA** (f), and USY (i).

patterns of all conventional zeolites showed several representative Bragg reflections, which matched well with those reported in the literature.[36–38] The crystals of conventional zeolites were similar to their bulk morphologies with smooth facets. The **MFI** zeolite morphology was represented as the aggregation of crystals with a diameters ranging from 50 to 150 nm. The **BEA** zeolite was composed of particles with a diameters ranging from 30 to 80 nm. Although the external surface of the particles showed crystal steps and terraces, the sorption analysis did not show the presence of mesopores. The nitrogen adsorption isotherms of zeolites **MFI** and **BEA** exhibited type I isotherm, which is typical for microporous materials (Figure 3). Therefore, both **MFI** and **BEA** zeolite samples possess very small external surface areas, compared with the NSZ samples (Table 1). The USY zeolite consists of rectangular prism-like

Table 1. Physicochemical Properties of NSZ-*x* samples (*x* = 22, 48, and 95), Conventional Zeolites (MFI, BEA, and USY), and Layered Zeolites (Lamellar MFI, Pillared MFI, and Self-Pillared MFI)

catalyst	Si/Al[a]	S_{BET}[b] (m^2 g^{-1})	S_{ext}[c] (m^2 g^{-1})	V_{tot}[d] (cm^3 g^{-1})
NSZ-22	22	540	360	0.63
NSZ-48	48	510	350	0.56
NSZ-95	95	610	370	0.62
MFI	12	300	67	0.16
BEA	13	670	180	0.20
USY	15	770	125	0.93
lamellar **MFI**	55	520	270	0.36
pillared **MFI**	52	610	490	0.51
self-pillared **MFI**	58	540	420	0.73

[a]Si/Al molar ratio obtained from ICP-AES elemental analysis. [b]S_{BET} is the BET surface area obtained from N_2 adsorption in relative pressure range (P/P_0) of 0.05–0.20. [c]S_{ext} is the external surface area evaluated from the *t*-plot method. [d]V_{tot} is the total pore volume obtained at P/P_0 = 0.95.

crystals with a wide distribution of diameters ranging from 200 to 500 nm. The particles possess mesopores with a broad pore-size distribution, which were generated by steam dealumination treatment. The nitrogen adsorption of USY zeolite was a combination of type I and IV with hysteresis loop due to the mesopores in the zeolite crystals (Figure 3). Physicochemical properties determined by nitrogen adsorption for all mentioned samples are shown in Table 1.

Figure 4 shows TEM images and XRD patterns of layered-type **MFI** zeolites. These **MFI** zeolites with various layered morphologies were prepared by synthesis procedures reported in the literature.[27–29] The zeolites samples denoted as "lamellar **MFI**", "pillared **MFI**", and "self-pillared **MFI**", according to the characteristic morphologies and the preparation methods. All layered zeolites exhibited the characteristic Bragg reflections corresponding to the typical **MFI** zeolite topology. The lamellar **MFI** sample was composed of exfoliated nanosheets with 2 nm thickness. The pillared **MFI** sample was supported by amorphous silica pillars, forming an ordered multilamellar **MFI** zeolite. The self-pillared **MFI** sample was assembled irregularly into a loose stacking of separate single-unit-cell-thick layers. The textural properties of these layered zeolites were evaluated by nitrogen adsorption isotherm (Figure 4). The nitrogen adsorption isotherm showed typical type IV with hysteresis loops. For lamellar **MFI** and self-pillared **MFI**, the hysteresis loops showed general type H3, which results in a broad distribution of mesopore diameters. In the case of pillared **MFI**, the hysteresis loop is of general type H4 due to ordered mesostructure. Thus, pillared **MFI** had high external surface area with uniform mesopores, compared with lamellar and self-pillared **MFI** zeolites.

The Si/Al ratios of all zeolites samples based on the elemental analysis using ICP-AES are shown in Table 1. The concentration and type of acid sites in the individual zeolites were determined by FTIR spectroscopy using pyridine as a probe molecule. Pyridine with a kinetic diameter of about 0.5 nm can enter the 10-ring channels (0.51 × 0.55 and 0.53 × 0.55 nm) of the **MFI** zeolite. The number of external Brønsted acid

DOI: 10.1021/cs502021a
ACS Catal. 2015, 5, 2596–2604

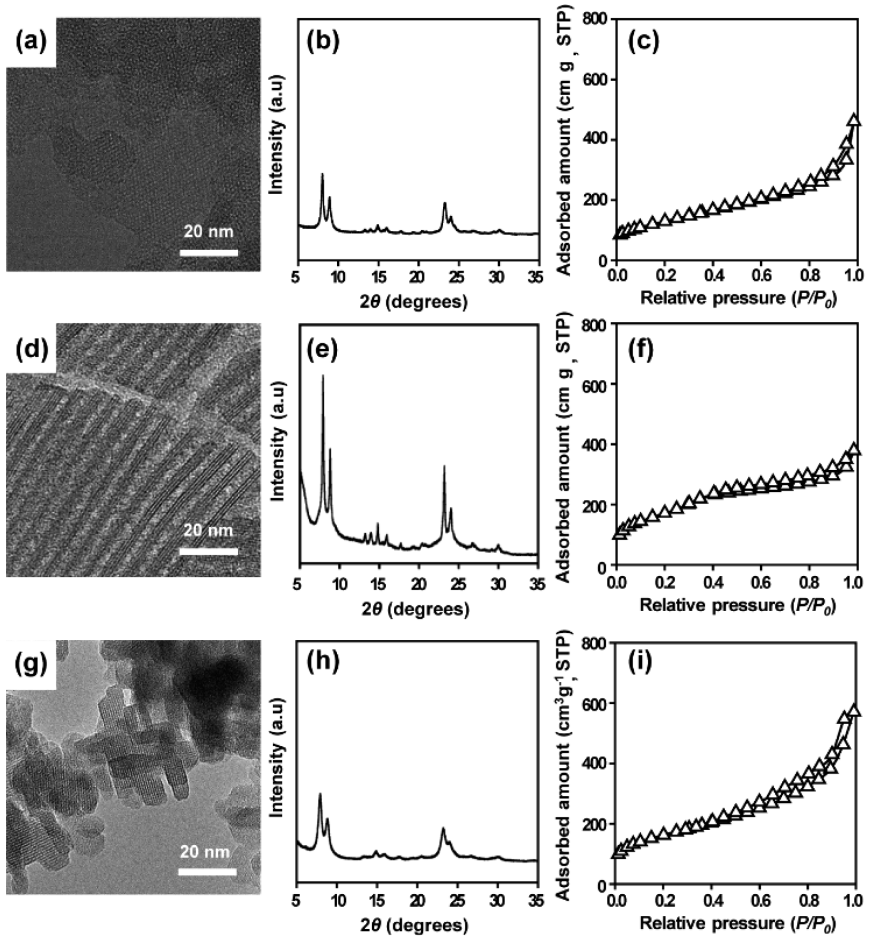

Figure 4. TEM images of lamellar **MFI** (a), pillared **MFI** (d), and self-pillared **MFI** (g). Powder XRD patterns of lamellar **MFI** (b), pillared **MFI** (e), and self-pillared **MFI** (h). Nitrogen adsorption of lamellar **MFI** (c), pillared **MFI** (f), and self-pillared **MFI** (i).

Table 2. Concentrations of Acid Sites in NSZ-*x* Samples (*x* = 22, 48, and 95), Conventional Zeolites (MFI, BEA, and USY), and Layered Zeolites (Lamellar MFI, Self-Pillared MFI, and Self-Pillared MFI) Measured by Pyridine and 2,6-Di-*tert*-butylpyridine (DTBP) Adsorption

	pyridine (mmol g^{-1})			DTBP (mmol g^{-1})				
catalyst	c_L	c_B	c_Σ	c_{B-S}	c_{L-S}[a]	$c_{\Sigma-S}$[b]	c_{B-S}/c_B (%)	$c_{L-S}/c_{\Sigma-S}$ (%)
NSZ-22	0.133	0.122	0.255	0.049	0.053	0.102	40	52
NSZ-48	0.072	0.087	0.159	0.042	0.035	0.076	48	46
NSZ-95	0.038	0.076	0.114	0.024	0.012	0.036	32	33
MFI	0.201	0.619	0.820	0.005	0.002	0.007	0.8	25
BEA	0.280	0.311	0.591	0.280	0.280	0.591	90	47
USY	0.340	0.200	0.540	0.202	0.340	0.540	100	63
lamellar **MFI**	0.090	0.117	0.207	0.041	0.030	0.072	35	42
pillared **MFI**	0.109	0.090	0.199	0.021	0.025	0.046	23	54
self-pillared **MFI**	0.058	0.151	0.209	0.030	0.011	0.042	20	26

[a]Calculating according to eq $c_{L-S} = c_L \times (c_{B-S}/c_B)/100$, assuming that fraction of surface Lewis acid sites is equal to the part of surface Brønsted acid centers (c_{B-S}/c_B), determined based on DTBP adsorption. [b]Calculating according to eq $c_{\Sigma-S} = c_{L-S} + c_{B-S}$.

sites was evaluated by FTIR, adsorbing 2,6-di-*tert*-butylpyridine (DTBP) onto the external surface of **MFI** zeolite. The DTBP is too bulky (0.8 nm) to enter the micropores of the **MFI** zeolite and hence can only be adsorbed on the acid sites located at the zeolite external surface.[39] Table 2 shows the concentrations of Brønsted and Lewis acid sites obtained in this manner.

The NSZ-22 sample possessed significantly higher amounts of total Brønsted and Lewis acid sites (0.122 and 0.133 mmol g^{-1}, respectively) than NSZ-48 (0.087 and 0.072 mmol g^{-1}, respectively) and NSZ-95 (0.076 and 0.038 mmol g^{-1}, respectively) samples. This result is in good agreement with the Al content of NSZ samples confirmed by ICP-AES. At the same time, all NSZ samples had a relatively large amount of Brønsted acid sites at the external surface, gradually decreasing with increase of Si/Al ratio (0.049, 0.042, and 0.024 mmol g^{-1} for NSZ-22, 48 and 95, respectively). The fractions of external Brønsted acid sites were quite high for all NSZ samples (32–48%) due to high external surface area of respective samples.

DOI: 10.1021/cs502021a
ACS Catal. 2015, 5, 2596–2604

On the other hand, the conventional **MFI** zeolite possessed a very small amount of external Brønsted acid sites (0.005 mmol g^{-1}, 0.8% of overall acid sites), compared with the NSZ samples. In the case of 12-ring zeolites (i.e., **BEA** and USY), DTBP molecules can penetrate into their micropore network and interact with the accessible Brønsted acid sites in the zeolite crystal. The highest values of Brønsted acid sites in **BEA** and USY zeolites were measurable for interaction with DTBP molecules (0.280 and 0.202 mmol g^{-1}, respectively). In agreement with previous reports, the results show high concentration of external Brønsted acid sites of layered **MFI** zeolites due to highly mesoporous properties (lamellar **MFI** = 0.041 mmol g^{-1}, pillared **MFI** = 0.021 mmol g^{-1} and self-pillared **MFI** = 0.030 mmol g^{-1}, respectively). The results indicate that NSZ-48 and layered zeolites possess similar concentrations of accessible Brønsted acid sites determined from DTBP adsorption.

Concentrations of the external Brønsted acid sites for pillared and self-pillared **MFI** zeolites equivalent to those used in the present work were also exhaustively compared in ref 29. Noticeably, the fraction of surface acid centers determined in present study is lower (20−23%, Table 2) than that found in ref 29 (30−45%). This inconsistency may be connected with a different basicity of probe molecules used. In particular, although Py (pK_b = 8.8[40]) and DTBP (pK_b = 9.0[40]) were chosen as probe molecules in the present study, dimethyl ether (pK_b = 17.5) and DTBP were used in ref 29 to probe total concentration of Brønsted acid sites and external acid centers, respectively. It seems that the combination of strong base molecules with appropriate kinetic diameter (e.g., Py and DTBP) likely interacting even with weakest acid sites is the preferable choice, which excludes the underestimation in total acidity and accurate evaluation of the fraction of surface acid sites.

One can notice that the fraction of Lewis acid centers in hierarchical zeolites possessing **MFI** topology (33−55%) exceeds those characteristic for commercial **MFI** zeolite (25%). Apparently, this feature of NSZ samples may affect their catalytic behavior regarding the unique characteristics of Al Lewis sites promoting Pechmann condensation of less active phenols shown in ref 41.

3.2. Effect of Si/Al Ratio of NSZ in Catalytic Performance. The catalytic behavior of NSZ samples was investigated in the liquid-phase Pechmann condensation reaction of bulky phenols (pyrogallol and resorcinol) with ethyl acetoacetate (Figures 5 and 6). The results indicate that the pyrogallol conversion over NSZ-22 catalyst increased rapidly to 20% within 1 h of the initial reaction period. Then, the pyrogallol conversion over NSZ-22 gradually increased up to 100% without a significant deactivation of the catalyst. This trend was observed also for both NSZ-48 and NSZ-95 catalysts in the same reaction.

The pyrogallol conversion increased in the order of NSZ-95 < NSZ-48 < NSZ-22 according to the increasing concentration of acid sites of the NSZ samples (Table 2). During the whole reaction run, the NSZ catalysts showed high selectivity (80−90%) to the desired product, 7,8-hydroxy-4-methyl-coumarin (Figure 5b). Some amount of polymeric molecules, formed from the primary reaction product, was also detected (10−20%).

In the case of resorcinol, the results are very similar to those of pyrogallol (Figure 6a). The only difference is that the resorcinol conversions were lower than pyrogallol conversion,

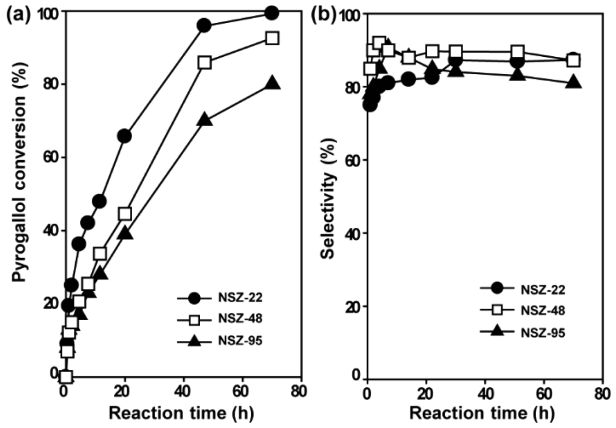

Figure 5. Conversion of pyrogallol (a) and selectivity (b) over NSZ-*x* samples (*x* = 22, 48, and 95) as a function of reaction time. Reaction conditions: 0.1 g of catalyst, 5 mmol of pyrogallol, 10 mmol of ethyl acetoacetate, 0.5 g of dodecane (internal standard), 10 mL of nitrobenzene (solvent), 423 K.

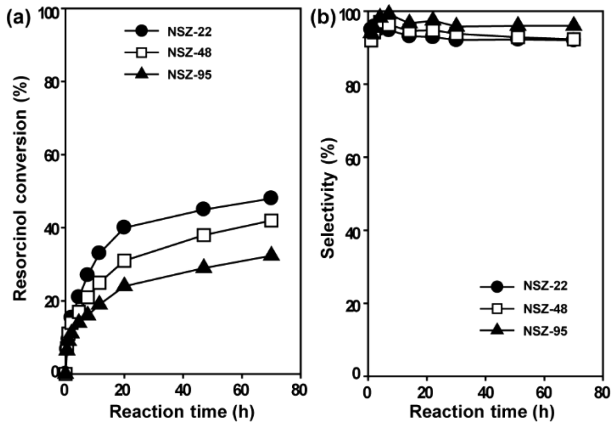

Figure 6. Conversion of resorcinol (a) and selectivity (b) over NSZ-*x* samples (*x* = 22, 48, and 95) as a function of reaction time. Reaction conditions: 0.1 g of catalyst, 5 mmol of resorcinol, 10 mmol of ethyl acetoacetate, 0.5 g of dodecane (internal standard), 10 mL of nitrobenzene (solvent), 423 K.

over all the NSZ catalysts. This can be explained by difference in the reactivity due to the mesomeric effect of the electron-donating substituents (e.g., hydroxyl group). Substitution for an additional hydroxyl group in phenyl ring make more active compounds for the Pechmann condensation reaction.

To investigate the catalytic performance of NSZ catalysts in more detail, additional catalytic reactions were performed under the same reaction condition, except that the reaction temperatures were varied from 393 to 423 K. At least three synthesized batches of NSZ samples were used as catalysts in the Pechmann condensation reaction. NSZ catalysts of different batches gave reproducible results within 5% relative errors in conversion during the entire measurements. The catalytic results at low reaction temperature (393 K) are shown in Figure S1. From these experiments, we calculated the number of reactant molecules converted per acid site per unit time (h) at the reaction time of 1 h, based on the total concentration of acid sites accessible for bulky DTBP molecules (Table 2). This value is denoted by "RPA", which stands for 'reaction rate per acid site'. We also calculated the total number of reactant molecules converted per acid site during 70 h. This is denoted

DOI: 10.1021/cs502021a
ACS Catal. 2015, 5, 2596−2604

by "NPA", which indicates 'number of molecules per acid site' of NSZ catalysts. Figures 7 and S2 show the RPA and NPA values of NSZ catalysts in Pechmann condensation reaction of pyrogallol and resorcinol at 393 and 423 K, respectively.

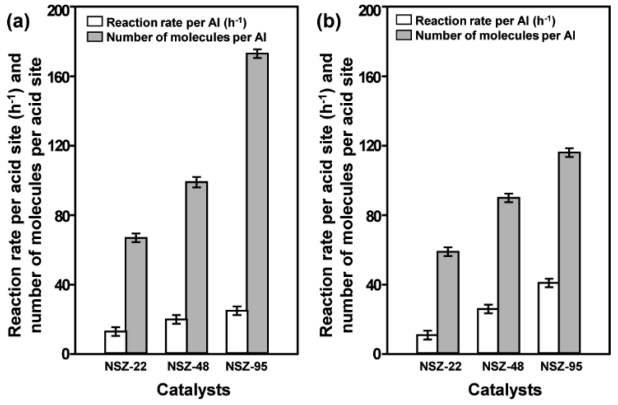

Figure 7. Reaction rate per acid site and number of molecules per acid site of NSZ-*x* samples (*x* = 22, 48, and 95) in the Pechmann condensation reaction of (a) pyrogallol and (b) resorcinol with ethyl acetoacetate. Reaction conditions: 0.1 g of catalyst, 5 mmol of phenols, 10 mmol of ethyl acetoacetate, 0.5 g of dodecane (internal standard), 10 mL of nitrobenzene (solvent), 393 K, 70 h. Error bars are represent the standard deviation calculated from a set of three different measurements.

For pyrogallol, both the RPA and NPA values increased in the order of NSZ-22 (RPA = 13 h^{-1}, NPA = 67) < NSZ-48 (20, 99) ≤ NSZ-95 (25, 173) (Figure 7a). Such tendency of decreasing catalytic activities with increasing Al content is common in zeolite acid catalysis, which can be attributed to the close location of Al sites. In the case of resorcinol, the results are also very similar to the result for pyrogallol (Figure 7b). The NSZ-48 (RPA = 26 h^{-1}, NPA = 90) and NSZ-95 (41, 116) catalysts exhibited higher RPA and NPA values than NSZ-22 (11, 59) in this reaction. The high RPA and NPA of NSZ with low Al containing catalysts indicate that the amount and location of Al sites are important to catalyze the Pechmann condensation reaction.

3.3. Comparison of Catalytic Performance of NSZs and Conventional Zeolites in the Pechmann Reaction. We have shown in the previous section that the NSZ catalyst with low Al concentration exhibited high catalytic activity per acid site (i.e., RPA and NPA) likely due to hydrophobicity effect in NSZ.

For comparison, we performed the Pechmann condensation reaction of pyrogallol and resorcinol over conventional **MFI**, **BEA**, and USY zeolites in order to investigate the effect of zeolite topology and pore architecture on the catalytic efficiency. The commercial **MFI** zeolite catalyst showed a negligible yield of target coumarin (Figure S3). This low catalytic performance is probably attributed to diffusion limitations into the micropores of **MFI** zeolite, whereas the micropore apertures of **MFI** (0.51 × 0.55 and 0.53 × 0.56 nm) are not sufficiently wide for the diffusion of reactants (kinetic diameter of pyrogallol = 0.71 nm) and product. Therefore, only a small fraction of acid sites on the external surface of MFI zeolite (0.007 mmol g^{-1}, Table 2) promotes Pechmann reaction under investigation. In the case of USY and especially **BEA** zeolite, the yield increased significantly (Figure S3). Better performance of **BEA** and USY zeolites compared with **MFI** could be explained by a higher concentration of acid sites involved in catalytic reaction occurring within large micropores of BEA (0.66 × 0.67 and 0.56 × 0.56 nm) and USY (0.74 × 0.74 nm) zeolites. Noticeably, the USY zeolite possessing mesopores facilitating the transport of reagents exhibited lower yield than **BEA** zeolite. It may be attributed to limited access to active centers located inside the large crystal of the USY zeolite (200−500 nm, Figure 3). On the other hand, NSZ-22 catalyst possessing lower concentration of acid sites showed high yield as compared with conventional zeolites. These results are attributed to high concentration of external acid sites and high external surface area, resulting in the facile diffusion of reactants and products before micropore blocking by coking.

For this reaction, RPA and NPA increased in the order of USY (RPA = 2 h^{-1}, NPA = 12) < **BEA** (1, 20) < **MFI** (9, 32) < NSZ-22 (13, 67). Figure 8b summarizes the results of the RPA and NPA in the same reaction of resorcinol, showing a similar tendency with the results in the pyrogallol condensation.

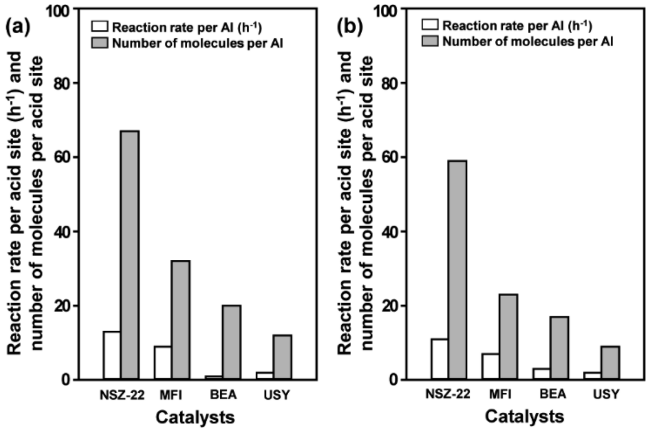

Figure 8. Reaction rate per acid site and number of molecules per acid site of NSZ-22 and conventional zeolites (**MFI**, **BEA** and USY) in the Pechmann condensation reaction of (a) pyrogallol and (b) resorcinol with ethyl acetoacetate. Reaction conditions: 0.1 g of catalyst, 5 mmol of phenols, 10 mmol of ethyl acetoacetate, 0.5 g of dodecane (internal standard), 10 mL of nitrobenzene (solvent), 393 K, 70 h.

Noticeably, the RPA values calculated for commercial MFI (RPA = 9) and NSZ-22 (RPA = 13) zeolites are closer if compared with commercial BEA (RPA = 1) and USY (RPA = 2) zeolites (Figure 8). This result can be attributed to the similar nature of active sites (acid centers located on the outer surface of catalysts' crystals) promoting Pechmann reaction over MFI zeolites. At the same time, 2-fold higher NPA value characteristic for NSZ-22 (NPA = 67) than commercial MFI zeolite (NPA = 32) may be connected with noticeably higher fraction of Lewis active centers in hierarchical zeolite (Table 2) and slower rate of NSZ-22 deactivation. Significantly lower values of RPA and NPA calculated for BEA and USY possessing acid centers of similar strength may indicate that either (1) not all acid sites detectable with DTBP are involved in reaction (e.g., diffusional limitations exist in the pore system of the catalysts) or (2) deactivation of active sites in BEA and USY catalysts over time (e.g., blocking of micropores with byproducts such as polycyclic aromatic compounds).

The Pechmann condensation reaction was also performed using **MFI** zeolites with layered morphology (e.g., lamellar, pillared, and self-pillared zeolite) as catalysts. Figure 9a shows RPA and NPA values of the catalysts in the pyrogallol

DOI: 10.1021/cs502021a
ACS Catal. 2015, 5, 2596−2604

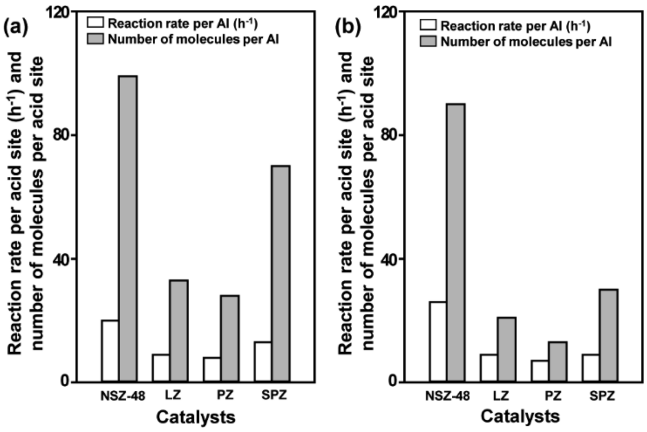

Figure 9. Reaction rate per acid site and number of molecules per acid site of NSZ-48 and layered zeolites (lamellar **MFI**, pillared **MFI**, and self-pillared **MFI**) in the Pechmann condensation reaction of (a) pyrogallol and (b) resorcinol with ethyl acetoacetate. Reaction conditions: 0.1 g of catalyst, 5 mmol of phenols, 10 mmol of ethyl acetoacetate, 0.5 g of dodecane (internal standard), 10 mL of nitrobenzene (solvent), 393 K, 70 h.

condensation. The catalytic performance increased in the order of pillared **MFI** (RPA = 8 h^{-1}, NPA = 28) < lamellar **MFI** (9, 33) < self-pillared **MFI** (13, 70) <NSZ-48 (20, 99).

The activity increase is consistent with shortening diffusion path lengths for self-pillared **MFI** and NSZ-48 catalyst if compared with lamellar and pillared **MFI**. Indeed, the most active self-pillared **MFI** and NSZ-48 catalysts are characterized by larger mesopores than lamellar and pillared **MFI** samples (Figure S4), assumedly having mass-transfer limitations in Pechmann reaction. Noticeably, self-pillared zeolite has a broad pore size distribution, but its pore sizes are the same or larger than those present in the NSZ-48 zeolite. Thus, despite having diffusion preferences, self-pillared **MFI** (RPA = 13, NPA = 70) appeared to be not as active as NSZ-48 (RPA = 20, NPA = 99). The reason may be a distinctly higher fraction of Lewis acid centers accessible for activation of substrates in NSZ-48 ($c_{L-S}/c_{\sum-S}$ = 46%, Table 2) versus self-pillared **MFI** ($c_{L-S}/c_{\sum-S}$ = 26%, Table 2). In addition, the difference in external surface activity of hierarchical MFI zeolites in Pechmann condensation reaction may be connected with different morphologies of zeolite domains for each catalyst as well as with other factors like surface roughness, surface defects, and aluminum distribution, as discussed in ref 42.

RPA and NPA in the resorcinol condensation reaction over all layered zeolite catalysts showed lower values in comparison with Pechmann reaction of pyrogallol being more reactive substrate (Figure 9b).

3.4. Recycle Test. We investigated the recyclability of NSZ catalysts in the Pechmann condensation reaction of pyrogallol and resorcinol with ethyl acetoacetate. Before recycle test of the catalyst, organic species, which result in the catalyst deactivation by pore blocking, in the NSZ-22 were analyzed after pyrogallol condensation for 30 h. The organic deposit in NSZ-22 was confirmed as various polymeric aromatic compounds by GC-mass spectroscopy. The polymeric aromatics are likely to be generated via side reaction routes, such as further condensation reaction of products inside the mesopores of NSZ-22 catalyst. However, this polymeric aromatic species could easily be removed by calcination in air atmosphere. Although uncalcined NSZ-22 showed negligible conversion of pyrogallol in the second cycle, the catalyst recovered its initial activity almost completely after regeneration (Table 3).

Table 3. Recyclability Test of NSZ-22 in the Pechmann Condensation Reaction[a] of Pyrogallol with Ethyl Acetoacetate

cycle	conversion (%)	selectivity (%)
1	42.5	89.5
2	41.6	88.3
3	41.2	90.1
4	41.0	90.0
5	40.1	87.4

[a]Reaction conditions: 0.1 g of catalyst, 5 mmol of pyrogallol, 10 mmol of ethyl acetoacetate, 0.5 g of dodecane (internal standard), 10 mL of nitrobenzene (solvent), 393 K.

The recovered NSZ-22 catalyst exhibited 95% of its original activity even after five cycles of the reaction. This recyclability of NSZ-22 could be explained by the high chemical and thermal stability of crystalline **MFI** zeolite with mesoporous structure. The XRD patterns of fresh and used NSZ-22 catalysts are shown in Figure S5. This result showed that there was no difference between the fresh and used NSZ-22 catalysts in the XRD patterns. This indicated the preservation of the crystallinity of NSZ-22 during the reaction−regeneration process. Thus, the large amount of acid sites on the external surface of NSZ-22 catalyst could be easily regenerated by calcination process (Figure S6).

4. CONCLUSIONS

We investigated the Pechmann condensation reaction of pyrogallol and resorcinol with ethyl acetoacetate over nanosponge **MFI** zeolite in comparison with conventional zeolites (**MFI**, **BEA**, and USY) and other layered **MFI**-based materials (lamellar, pillared, and self-pillared **MFI**). The nanosponge catalysts exhibited the best catalytic performance in the liquid-phase condensation reactions among all the investigated zeolites. Thus, nanosponge **MFI** zeolite can be useful in a wide range of liquid-phase reactions, which involve bulky species. The high catalytic performance of the nanosponge compared with bulk zeolites can naturally be attributed to a large number of acid sites located on external surfaces, so that bulky-molecular reactions can be catalyzed without diffusion limitations. However, its difference from other layered-type **MFI** zeolites is an intriguing result, indicating that acid catalytic sites on external surfaces of these zeolites could exhibit more or less different catalytic functions depending on their morphology.

■ ASSOCIATED CONTENT

Supporting Information

The following file is available free of charge on the ACS Publications website at DOI: 10.1021/cs502021a.

Supplemental data as noted in the text (PDF)

■ AUTHOR INFORMATION

Corresponding Author

*E-mail: jiri.cejka@jh-inst.cas.cz. Tel.: (+420) 26605 3795. Fax: (+420) 28658 2307.

DOI: 10.1021/cs502021a
ACS Catal. 2015, 5, 2596−2604

Notes

The authors declare no competing financial interest.

■ ACKNOWLEDGMENTS

J.Č. acknowledges the Czech Science Foundation for the support of this research (P106/12/0189). R.R. acknowledges the Institute for Basic Science (IBS-R004-D1).

■ REFERENCES

(1) Sethna, S.; Phadke, R. In *Organic Reactions*; Denmark, S. E., Aubé, J., Cha, J. K., Farina, V., Feldman, P., Hall, D., Hergenrother, P. J., Johnson, J. S., Kozlowski, M. C., Molander, G., Montgomery, J., Rovis, T., Weinreb, S. M., Eds.; John Wiley & Sons, Inc.: New York, 2011; pp 1−58.
(2) Gunnewegh, E. A.; Hoefnagel, A. J.; Downing, R. S.; vanBekkum, H. *Recl. Trav. Chim. Pays-Bas* **1996**, *115*, 226−230.
(3) Sun, W. C.; Gee, K. R.; Haugland, R. P. *Bioorg. Med. Chem. Lett.* **1998**, *8*, 3107−3110.
(4) Oyamada, J.; Jia, C. G.; Fujiwara, Y.; Kitamura, T. *Chem. Lett.* **2002**, *31*, 380−381.
(5) Daru, J.; Stirling, A. *J. Org. Chem.* **2011**, *76*, 8749−8755.
(6) Woods, L. L.; Sapp, J. *J. Org. Chem.* **1962**, *27*, 3703−3705.
(7) Gupta, A. K. D.; Chatterje, R. M.; Das, K. R.; Green, B. *J. Chem. Soc. C* **1969**, 29−33.
(8) Canter, F. W.; Curd, F. H.; Robertson, A. *J. Chem. Soc.* **1931**, 1245−1255.
(9) Horning, E. C.; Horning, M. G.; Dimmig, D. A. In *Organic Syntheses*; John Wiley & Sons, Inc.: New York, 2003.
(10) Gunnewegh, E. A.; Hoefnagel, A. J.; vanBekkum, H. *J. Mol. Catal. A: Chem.* **1995**, *100*, 87−92.
(11) Chaudhari, D. D. *Chem. Ind.* **1983**, 568−569.
(12) Sabou, R.; Hoelderich, W. F.; Ramprasad, D.; Weinand, R. *J. Catal.* **2005**, *232*, 34−37.
(13) Torviso, R.; Mansilla, D.; Belizan, A.; Alesso, E.; Moltrasio, G.; Vazquez, P.; Pizzio, L.; Blanco, M.; Caceres, C. *Appl. Catal., A* **2008**, *339*, 53−60.
(14) Sudha, S.; Venkatachalam, K.; Priya, S. V.; Mabel, J. H.; Palanichamy, M.; Murugesan, V. *J. Mol. Catal. A: Chem.* **2008**, *291*, 22−29.
(15) Tyagi, B.; Mishra, M. K.; Jasra, R. V. *J. Mol. Catal. A: Chem.* **2007**, *276*, 47−56.
(16) Shamzhy, M.; Opanasenko, M.; Shvets, O.; Cejka, J. *Front. Chem.* **2013**, *1*, 1−11.
(17) Opanasenko, M.; Shamzhy, M.; Cejka, J. *ChemCatChem* **2013**, *5*, 1024−1031.
(18) Choi, M.; Na, K.; Kim, J.; Sakamoto, Y.; Terasaki, O.; Ryoo, R. *Nature* **2009**, *461*, 246−249.
(19) Jo, C.; Cho, K.; Kim, J.; Ryoo, R. *Chem. Commun.* **2014**, *50*, 4175−4177.
(20) Jo, C.; Seo, Y.; Cho, K.; Kim, J.; Shin, H. S.; Lee, M.; Kim, J.-C.; Kim, S. O.; Lee, J. Y.; Ihee, H.; Ryoo, R. *Angew. Chem., Int. Ed.* **2014**, *53*, 5117−5121.
(21) Kim, J.-C.; Lee, S.; Cho, K.; Na, K.; Lee, C.; Ryoo, R. *ACS Catal.* **2014**, *4*, 3919−3927.
(22) Kim, J.-C.; Cho, K.; Ryoo, R. *Appl. Catal., A* **2014**, *470*, 420−426.
(23) Opanasenko, M. V.; Shamzhy, M. V.; Jo, C.; Ryoo, R.; Cejka, J. *ChemCatChem* **2014**, *6*, 1919−1927.
(24) Ramos, F. S. O.; de Pietre, M. K.; Pastore, H. O. *RSC Adv.* **2013**, *3*, 2084−2111.
(25) Roth, W. J.; Nachtigall, P.; Morris, R. E.; Čejka, J. *Chem. Rev.* **2014**, *114*, 4807−4837.
(26) Diaz, U.; Corma, A. *Dalton Trans.* **2014**, *43*, 10292−10316.
(27) Na, K.; Choi, M.; Park, W.; Sakamoto, Y.; Terasaki, O.; Ryoo, R. *J. Am. Chem. Soc.* **2010**, *132*, 4169−4177.
(28) Na, K.; Park, W.; Seo, Y.; Ryoo, R. *Chem. Mater.* **2011**, *23*, 1273−1279.
(29) Zhang, X.; Liu, D.; Xu, D.; Asahina, S.; Cychosz, K. A.; Agrawal, K. V.; Al Wahedi, Y.; Bhan, A.; Al Hashimi, S.; Terasaki, O.; Thommes, M.; Tsapatsis, M. *Science* **2012**, *336*, 1684−1687.
(30) Emeis, C. A. *J. Catal.* **1993**, *141*, 347−354.
(31) Camblor, M. A.; Corma, A.; García, H.; Semmer-Herlédan, V.; Valencia, S. *J. Catal.* **1998**, *177*, 267−272.
(32) Tao, Y. S.; Kanoh, H.; Abrams, L.; Kaneko, K. *Chem. Rev.* **2006**, *106*, 896−910.
(33) Kruk, M.; Jaroniec, M.; Kim, J. H.; Ryoo, R. *Langmuir* **1999**, *15*, 5279−5284.
(34) Imperor-Clerc, M.; Davidson, P.; Davidson, A. *J. Am. Chem. Soc.* **2000**, *122*, 11925−11933.
(35) Cranston, R. W.; Inkley, F. A. *Adv. Catal.* **1957**, *9*, 143−154.
(36) Newsam, J. M.; Treacy, M. M. J.; Koetsier, W. T.; Degruyter, C. B. *Proc. R. Soc. London, Ser. A* **1988**, *420*, 375−405.
(37) Janssen, A. H.; Koster, A. J.; de Jong, K. P. *J. Phys. Chem. B* **2002**, *106*, 11905−11909.
(38) Derouane, E. G.; Detremmerie, S.; Gabelica, Z.; Blom, N. *Appl. Catal.* **1981**, *1*, 201−224.
(39) Corma, A.; Fornes, V.; Forni, L.; Marquez, F.; Martinez-Triguero, J.; Moscotti, D. *J. Catal.* **1998**, *179*, 451−458.
(40) Kunkeler, P. J.; Downing, R. S.; Bekkum, H. v. In *Stud. Surf. Sci. Catal.*; H. van Bekkum, E. M. F. P. A. J., Jansen, J. C., Eds.; Elsevier: 2001; Vol. *137*, pp 987−1001.
(41) In *Name Reactions in Heterocyclic Chemistry II*; Li, J. J., Corey, E. J., Eds.; John Wiley & Sons, Inc.: New York, 2011; pp 457−458.
(42) Liu, D.; Zhang, X.; Bhan, A.; Tsapatsis, M. *Microporous Mesoporous Mater.* **2014**, *200*, 287−290.

DOI: 10.1021/cs502021a
ACS Catal. 2015, 5, 2596−2604